2023

UNCOVER: Illuminating the Early Universe—JWST/NIRSpec Confirmation of z > 12 Galaxies

Sam E. Cutler

John R. Weaver

Katherine E. Whitaker

et. al.

The Astrophysical Journal Letters, 957:L34 (13pp), 2023 November 10 https://doi.org/10.3847/2041-8213/acfe07

UNCOVER: Illuminating the Early Universe—JWST/NIRSpec Confirmation of $z > 12$ Galaxies

Bingjie Wang (王冰洁)[1,2,3], Seiji Fujimoto[4,21], Ivo Labbé[5], Lukas J. Furtak[6], Tim B. Miller[7,8], David J. Setton[9], Adi Zitrin[6], Hakim Atek[10], Rachel Bezanson[9], Gabriel Brammer[11], Joel Leja[1,2,3], Pascal A. Oesch[11,12], Sedona H. Price[9], Iryna Chemerynska[10], Sam E. Cutler[13], Pratika Dayal[14], Pieter van Dokkum[7], Andy D. Goulding[15], Jenny E. Greene[15], Y. Fudamoto[16,17], Gourav Khullar[9], Vasily Kokorev[14], Danilo Marchesini[18], Richard Pan[18], John R. Weaver[13], Katherine E. Whitaker[11,13], and Christina C. Williams[19,20]
[1] Department of Astronomy & Astrophysics, The Pennsylvania State University, University Park, PA 16802, USA; bwang@psu.edu
[2] Institute for Computational & Data Sciences, The Pennsylvania State University, University Park, PA 16802, USA
[3] Institute for Gravitation and the Cosmos, The Pennsylvania State University, University Park, PA 16802, USA
[4] Department of Astronomy, The University of Texas at Austin, Austin, TX 78712, USA
[5] Centre for Astrophysics and Supercomputing, Swinburne University of Technology, Melbourne, VIC 3122, Australia
[6] Department of Physics, Ben-Gurion University of the Negev, P.O. Box 653, Beer-Sheva 84105, Israel
[7] Department of Astronomy, Yale University, New Haven, CT 06511, USA
[8] Center for Interdisciplinary Exploration and Research in Astrophysics (CIERA) and Department of Physics & Astronomy, Northwestern University, IL 60201, USA
[9] Department of Physics & Astronomy and PITT PACC, University of Pittsburgh, Pittsburgh, PA 15260, USA
[10] Institut d'Astrophysique de Paris, CNRS, Sorbonne Université, 98bis Boulevard Arago, F-75014, Paris, France
[11] Cosmic Dawn Center (DAWN), Niels Bohr Institute, University of Copenhagen, Jagtvej 128, København N, DK-2200, Denmark
[12] Department of Astronomy, University of Geneva, Chemin Pegasi 51, 1290 Versoix, Switzerland
[13] Department of Astronomy, University of Massachusetts, Amherst, MA 01003, USA
[14] Kapteyn Astronomical Institute, University of Groningen, 9700 AV Groningen, The Netherlands
[15] Department of Astrophysical Sciences, Princeton University, Princeton, NJ 08544, USA
[16] Waseda Research Institute for Science and Engineering, Faculty of Science and Engineering, Waseda University, 3-4-1 Okubo, Shinjuku, Tokyo 169-8555, Japan
[17] National Astronomical Observatory of Japan, 2-21-1, Osawa, Mitaka, Tokyo, Japan
[18] Department of Physics & Astronomy, Tufts University, MA 02155, USA
[19] NSF's National Optical-Infrared Astronomy Research Laboratory, Tucson, AZ 85719, USA
[20] Steward Observatory, University of Arizona, Tucson, AZ 85721, USA
Received 2023 August 14; revised 2023 September 18; accepted 2023 September 28; published 2023 November 13

Abstract

Observations of high-redshift galaxies provide a critical direct test to the theories of early galaxy formation, yet to date, only three have been spectroscopically confirmed at $z > 12$. Due to strong gravitational lensing over a wide area, the galaxy cluster field A2744 is ideal for searching for the earliest galaxies. Here we present JWST/NIRSpec observations of two galaxies: a robust detection at $z_{\rm spec} = 12.393^{+0.004}_{-0.001}$, and a plausible candidate at $z_{\rm spec} = 13.079^{+0.013}_{-0.001}$. The galaxies are discovered in JWST/NIRCam imaging and their distances are inferred with JWST/NIRSpec spectroscopy, all from the JWST Cycle 1 UNCOVER Treasury survey. Detailed stellar population modeling using JWST NIRCam and NIRSpec data corroborates the primeval characteristics of these galaxies: low mass ($\sim 10^8 M_\odot$), young, rapidly assembling, metal-poor, and star-forming. Interestingly, both galaxies are spatially resolved, having lensing-corrected rest-UV effective radii on the order of 300–400 pc, which are notably larger than other spectroscopically confirmed systems at similar redshifts. The observed dynamic range of $z \gtrsim 10$ sizes spans over 1 order of magnitude, implying a significant scatter in the size–mass relation at early times. Deep into the epoch of reionization, these discoveries elucidate the emergence of the first galaxies.

Unified Astronomy Thesaurus concepts: Early universe (435); Galaxy formation (595); Galaxy spectroscopy (2171); High-redshift galaxies (734); James Webb Space Telescope (2291); Spectral energy distribution (2129)

1. Introduction

The cosmic dawn, marked by the emergence of the first stars that formed out of the pristine primordial gas, heralded the most recent global phase transition of the Universe: known as the epoch of reionization, it is a period where the first luminous sources ionized the neutral hydrogen that once pervaded the entire Universe. While there exist observational constraints coming from the Thomson scattering optical depth inferred from the cosmic microwave background (Hinshaw et al. 2013; Planck Collaboration et al. 2020) and quasar absorption lines (Fan et al. 2006; McQuinn 2016, and references therein) via the Gunn–Peterson effect (Gunn & Peterson 1965), the history and the drivers of reionization remain largely unknown (see Robertson 2022 for a recent review). Finding the earliest galaxies constitutes a key piece in constructing a coherent narrative of the cosmic history. Their properties would provide crucial insights into some of the longstanding questions of extragalactic astronomy: the nature of Population III stars, the coalescence of the first cosmic structures, and the seeds of supermassive black holes (see Bromm & Yoshida 2011; Inayoshi et al. 2020; Klessen & Glover 2023 for theoretical overviews).

The past decade has seen substantial advancements in the observations of galaxies at $6 < z < 10$, offering evidence for

[21] Hubble Fellow.

early star formation activities and their contribution to reionization (Madau & Dickinson 2014; Stark 2016). This progress has mainly been driven by the near-infrared (IR) sensitivity of the Wide Field Camera 3 (WFC3) onboard the Hubble Space Telescope (HST). The most distant known galaxy until recently was GN-z11 with a grism redshift of $z \sim 11$ (Oesch et al. 2016). The redshift frontier is now pushed farther back owing to the launch of the James Webb Space Telescope (JWST), whose NIRCam instrument extends our high-resolution IR coverage to ∼1–5 μm and also provides higher sensitivity than HST (Rigby et al. 2023). In addition to unambiguously establishing the spectroscopic redshift of GN-z11 at $z = 10.60$ (Bunker et al. 2023), several $z \gtrsim 10$ galaxies have been confirmed via NIRSpec (Arrabal Haro et al. 2023a, 2023b; RobertsBorsani et al. 2023; Fujimoto et al. 2023; Williams et al. 2023) and two at $z > 12$, the highest redshift among which is at $z = 13.20^{+0.04}_{-0.07}$ (Curtis-Lake et al. 2023; Robertson et al. 2023). The only other confirmed NIRCam-selected galaxy at $z \sim 12$ is based on an Atacama Millimeter/submillimeter Array (ALMA) detection of [O III] emission (Bakx et al. 2023). These discoveries provide some of the first direct insights into the astrophysical processes governing galaxy growth near the cosmic dawn.

Aided by strong gravitational lensing, the JWST Treasury Cycle 1 UNCOVER survey (Bezanson et al. 2022) turns the field containing the galaxy cluster A2744 at $z = 0.308$ into the deepest view of our Universe to date—the intrinsic depths of $\gtrsim$31–32 AB magnitudes make it ideal for carrying out searches for the first galaxies. In this Letter, we present two high-redshift galaxies discovered with UNCOVER spectroscopy. UNCOVER-z12 has a secure $z_{\rm spec} = 12.393^{+0.004}_{-0.001}$ due to an unambiguous Lyman break; UNCOVER-z13 is tentatively detected at $z_{\rm spec} = 13.079^{+0.013}_{-0.001}$. The lower signal-to-noise ratio (S/N) of the latter leads us to refrain from a highly confident $z > 13$ interpretation, although the probability density distribution of redshift, $p(z)$, sharply peaks at this high redshift.

The structure of this Letter is as follows. Section 2 provides an overview of the data, including imaging, candidate selection, and spectroscopy. Section 3 details the measurement of the spectroscopic redshift and of the morphology in the imaging. Section 4 explains the assumptions and components involved in fitting the spectral energy distribution (SED). Section 5 presents the results. Section 6 concludes with a summary of the key findings.

Where applicable, we adopt the best-fit cosmological parameters from the WMAP 9 yr results: $H_0 = 69.32$ km s^{-1} Mpc^{-1}, $\Omega_M = 0.2865$, and $\Omega_\Lambda = 0.7135$ (Hinshaw et al. 2013), and a Chabrier initial mass function (IMF; Chabrier 2003) over 0.1–100 $M_\odot$. Unless otherwise mentioned, we report the median of the posterior, and 1σ error bars are the 16th and 84th percentiles.

2. Data

2.1. Imaging

The reduction of all publicly available HST and JWST imaging over A2744 used herein is outlined in Bezanson et al. (2022). This comprises 15 broad- and medium-band filters from JWST/NIRCam, HST/ACS, and HST/WFC3, covering the wavelength range of ∼0.4–5μ m. The JWST/NIRCam observations originate from three programs: UNCOVER (PIs: Labbe and Bezanson, JWST-GO-2561; Bezanson et al. 2022), the Early Release Science program GLASS (PI: Treu, JWST-ERS-1324; Treu et al. 2022), and a Director's Discretionary program (PI: Chen, JWST-DD-2756), together providing eight filters: F090W, F115W, F150W, F200W, F277W, F356W, F410M, and F444W. The HST data, obtained from the public archive, include HST-GO-11689 (PI: Dupke), HST-GO-13386 (PI: Rodney), HST-DD-13495 (PI: Lotz; Lotz et al. 2017), and HST-GO-15117 (PI: Steinhardt; Steinhardt et al. 2020). These additional observations cover a wavelength range of ∼0.4–1.6 μm in the observed frame, using seven filters: F435W, F606W, F814W, F105W, F125W, F140W, and F160W.

Photometric catalogs are constructed for ∼50,000 objects identified from a noise-equalized detection image combining F277W, F356W, and F444W imaging, with aperture-corrected fluxes extracted with the `python` implementation of Source Extractor (Bertin & Arnouts 1996; Barbary et al. 2016) as described in Weaver et al. (2023). We use the latest photometry herein (internal release v3.0.0).[22] The photometric measurements for both sources are extracted within an aperture size of 0.″32 on images convolved to a uniform point-spread function.

For the lens model, we use an updated version of the Furtak et al. (2023) analytic model of A2744. This version[23] includes one additional multiple-image system in the northern substructure, and more importantly, an additional spectroscopic redshift in the northwestern substructure from new Very Large Telescope/MUSE observations of the cluster (Bergamini et al. 2023). These improvements bring the lens plane image reproduction rms of the model down to $\Delta_{\rm RMS} = 0.''51$.

2.2. Candidates

The sample consists of galaxies initially identified in HST + JWST imaging. UNCOVER-z12 is originally identified in Atek et al. (2023; ID 42329), with a photometric redshift at $z_{\rm phot} = 11.83^{+1.05}_{-7.93}$. The selection procedure combines dropout information from the color–color diagram, and photometric redshifts using the `EAzY` and `BEAGLE` software. In particular, a strong Lyman break (>1.5 AB mag) is required to meet the selection threshold. A secondary set of criteria addresses the quality of the photometric redshifts: here, $\chi^2 < 30$ combined with good agreement (within uncertainties) between `EAzY` and `BEAGLE` solutions is enforced. UNCOVER-z12 is assigned a quality flag of 3 mainly due to disagreements between the photometric redshift solutions (see Atek et al. 2023 for details).

UNCOVER-z13 is selected based on two main criteria. The first is the reliability of the photometry. This includes `use_phot` = 1 (see Weaver et al. 2023 for details on the flag), S/N > 7 in the long-wavelength filter bands, and having data in at least six NIRCam filter bands. Second, we require a robust high-redshift solution from the photometry, with a redshift posterior median at $z_{\rm phot} > 11$ and the 16th percentile of the redshift posterior >6 (i.e., a low probability of low-redshift interlopers). There is a final visual inspection for basic quality control before the allocation of NIRSpec slits. In addition, the `Prospector-`β model (Wang et al. 2023) within `Prospector` (Johnson et al. 2021) finds both candidates to have $z_{\rm phot} > 11$ (Wang et al. 2023).

[22] Since making the preprints available in early 2023, both the data reduction and photometric pipelines have improved significantly, details of which will be presented in the published versions of Bezanson et al. (2022) and Weaver et al. (2023).

[23] The `v1.1` deflection maps are publicly available on the UNCOVER website https://jwst-uncover.github.io/DR1.html#LensingMaps.

In total, there are eight $z > 11$ candidates followed up with spectroscopy, further details of which can be found in Appendix A. Low- and high-redshift galaxies possibly sharing similar photometric colors is a known challenge, and is exacerbated by the new redshift frontier in the era of JWST (Dunlop et al. 2007; Naidu et al. 2022a; Arrabal Haro et al. 2023a; McKinney et al. 2023; Zavala et al. 2023). The redshift calibration for the UNCOVER survey will be presented in a future paper.

2.3. NIRSpec/Prism Spectroscopy

The JWST/NIRSpec low-resolution Prism spectra presented in this paper were collected between 2023 July 31 and August 2 as part of the second phase of the UNCOVER Treasury survey (Bezanson et al. 2022). This Letter is based on internal v0.3 reductions. The full spectroscopic data reduction and extraction will be presented in S. Price et al. (2023), in preparation. We summarize, briefly, as follows. These NIRSpec/MSA observations are separated into seven semioverlapping footprints with some repeated targets, yielding on-source integration times of between 2.7 and 17.4 hr. Overall integration times for the current targets are 4.4 hr (38766, MSA4) and 7.4 hr (13077, MSA5 and MSA7). All sources were assigned three-slitlets and observations were conducted with a `2-POINT-WITH-NIRCam-SIZE2` dither pattern.

Stage 2 data products were downloaded from MAST reduced with `msaexp` (v0.6.10; Brammer et al. 2022), `msaexp` masks artifacts (including snowballs), and corrects for $1/f$ noise. Individual slits are identified and WCS solutions are applied, data are flat fielded, and background subtracted (from vertically shifted spectra). The 2D spectra are stacked and drizzled together and then optimally extracted. We also perform an additional manual extraction on UNCOVER-z13 as a complementary quality control. Both 1D and 2D spectra are included in Figure 1.

3. Data Analyses

3.1. Spectroscopic Redshifts

Spectroscopic redshifts are determined using `msaexp`, which finds the best-fit redshift by minimizing the χ^2 between a template set and the observed spectrum. We choose the `blue_sfhz_13` template made available as a part of the `EAzY` code package (Brammer et al. 2008). This template set forbids unphysical star formation histories (SFHs) that are older than the age of the Universe at a given redshift, making it more suitable for our application. At $z \gtrsim 10$, the strongest feature to secure a redshift solution is the Lyman break. Emission lines are also identified and contribute to the likelihood. The attenuation of the intergalactic medium (IGM) is assumed to follow Inoue et al. (2014), and the damping Lyα wing is also considered (e.g., Arrabal Haro et al. 2023b; Curtis-Lake et al. 2023). We allow the search for the minimal χ^2 value over the full range of $0.1 \leqslant z \leqslant 20$. Uncertainties are from the 68.2% range of the integrated $p(z)$. In addition, we characterize the break strength by comparing the mean of the flux in two segments over 150 Å blue- and redward of the observed break.

3.2. Morphology

Morphology measurements are performed using `pysersic` (Pasha & Miller 2023) assuming a Sérsic profile for each source and a flat background that is fit simultaneously. Priors for $r_{\rm eff}$, $n_{\rm Sersic}$, and the axis ratio are flat and bounded by 0.5–10 pixels, 0.65–4, and 0.1–1, respectively; priors for the central position and fluxes are Gaussian and based on the measurements from the photometric catalog. The posteriors for all variables are explored using the No U-turn Sampler (NUTS; Hoffman & Gelman 2011; Phan et al. 2019) where two chains are run for 1000 warm-up iterations followed by 1000 sampling steps each.

Additionally, we model UNCOVER-z12 with two Sérsic components. The priors in this case are independent and similar to the above, except for the flux. We assume each source has half of the catalog flux, and the central positions are offset by about two pixels in the northwest (NW) and southeast (SE) direction, respectively.

Our morphology measurements focus on F277W as this leads to the best constraints for both sources, owing to the higher S/N. It is worth noting that at the redshifts measured, the rest-frame wavelength of the F277W filter is in the far-ultraviolet, which is expected to trace recent ($\lesssim$20 Myr) unobscured star formation. We also perform Sérsic fits in the redder F444W filter, which give similar results for UNCOVER-z12. However, given the faintness of UNCOVER-z13 in the redder bands, the fits for this source yield limited constraints.

4. SED Fitting

4.1. Prospector

The available JWST/NIRCam and HST/ACS WFC3 photometry are jointly fitted with the full NIRSpec/Prism spectrum with an 18-parameter model within the `Prospector` inference framework (Johnson et al. 2021). Before fitting, all models are convolved with the NIRSpec/Prism instrumental resolution curve,[24] assuming that the flight performance is 1.3 times better than stated. This accounts for the fact that the spatial extent of the sources in the dispersion direction is narrower than the shutter width, and is consistent with an earlier work where a factor 1/0.7 is introduced for modeling $z > 10$ galaxies with `BEAGLE` (Curtis-Lake et al. 2023). As the spectral calibration is at an early stage, we fit for a polynomial calibration vector of order 2 after applying a wavelength-independent calibration to scale the normalization of the spectrum to the photometry.

We follow the same methodology as detailed in the paper presenting the UNCOVER stellar populations catalog (Wang et al. 2023), with the exception that the redshift is restricted to vary in a narrow range around the best-fitting spectroscopic redshifts ($\pm$0.1) determined by `msaexp` based on `EAzY` templates. Here we briefly reiterate the modeling process for completeness.

All parameters are inferred jointly, using the MIST stellar isochrones (Choi et al. 2016; Dotter 2016) and MILES (Sánchez-Blázquez et al. 2006) stellar spectral library in FSPS (Conroy & Gunn 2010). The SFH is described by the nonparametric `Prospector-`α model via mass formed in seven logarithmically spaced time bins (Leja et al. 2017). A mass function prior, and a dynamic SFH (M, z) prior are included to optimize the photometric inference over the wide parameter space covered by deep JWST surveys (Wang et al. 2023). Lensing magnification using the publicly released maps (Furtak et al. 2023) is performed on the fly (i.e., $\mu = \mu(z)$) to

[24] `jwst_nirspec_Prism_disp.fits` provided by the Space Telescope Science Institute.

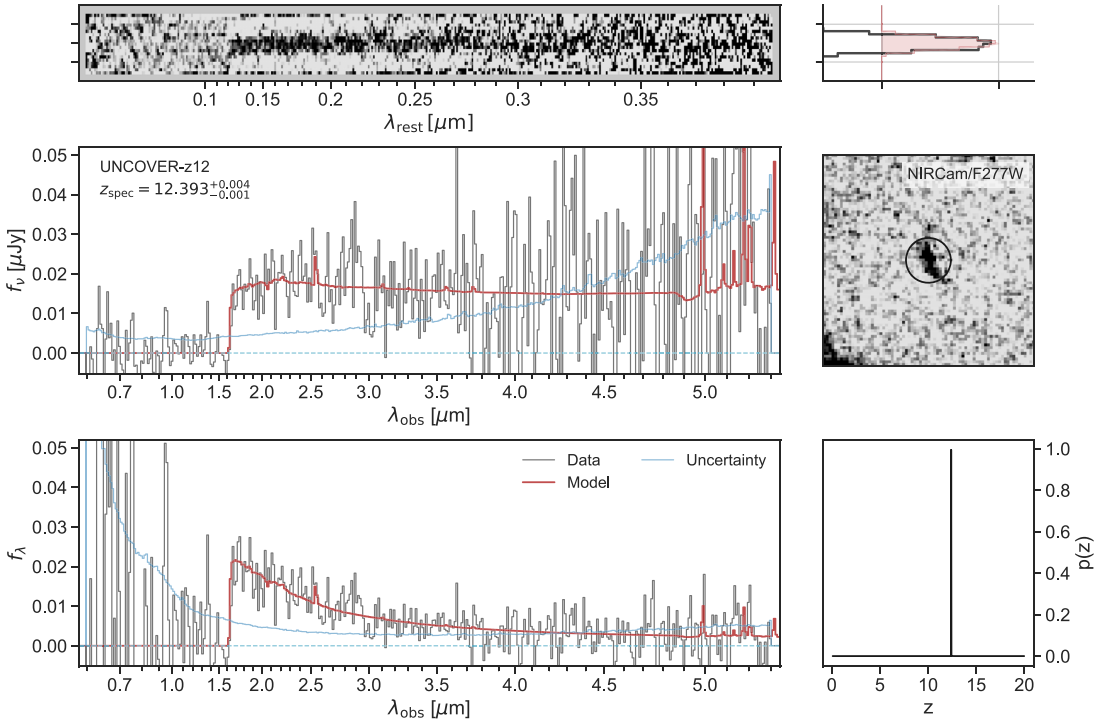

(a)

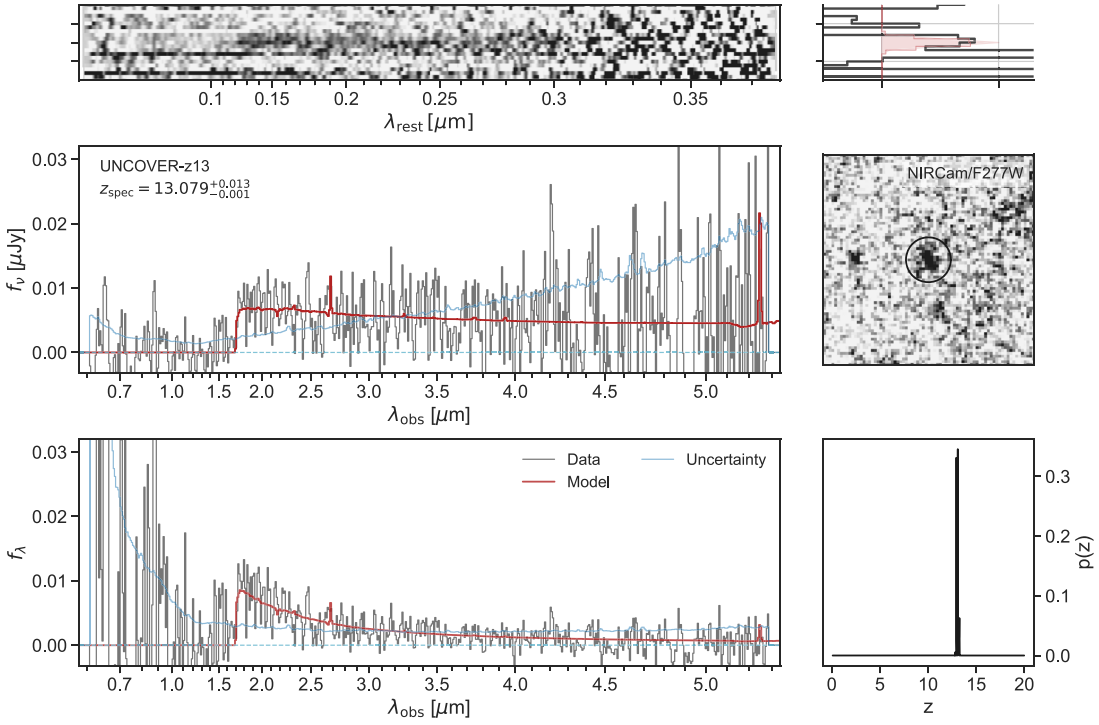

(b)

Figure 1. NIRSpec/Prism observations of the two galaxies presented in this Letter. (a) The first row displays the 2D spectrum of UNCOVER-z12, with the rest-frame wavelength shown along the x-axis; the histogram indicates the extracted region. Second row, left panel, shows the 1D spectrum in f_ν as a function of the observed wavelength. Data are plotted in gray, whereas the best-fit `EAzY` model is plotted in red. Also plotted are the uncertainties in blue. The cyan horizontal line is at $y = 0$ to guide the eye. Second row, right panel, includes the cutout in the F277W band, with the circle indicating the aperture size, $0\farcs32$, in which photometry is extracted. Third row, left panel, shows the 1D spectrum again, but in f_λ as a complementary visualization. Third row, right panel, plots the probability density over the redshift range of the search for a minimum χ^2. A strong Lyman break is clearly seen for UNCOVER-z12. (b) Same as the above figure set, but for UNCOVER-z13. We err on the conservative side and consider its redshift solution to be less well-determined due to the weaker break, even though $p(z)$ sharply peaks at $z > 12$.

ensure consistency with the scale-dependent priors. Because of the lack of emission lines observed, we do not turn on the emission-line marginalization. A 5% error floor is imposed on the photometry to account for systematics. Sampling is performed using the dynamic nested sampler `dynesty` (Speagle 2020).

4.2. Bagpipes

We also perform spectrophotometric modeling using the Bayesian Analysis of Galaxies for Physical Inference and Parameter EStimation (`Bagpipes`) software package (Carnall et al. 2018, 2019). The following model grid is utilized: Bruzual & Charlot's (2003) stellar population models, the MILES spectral library (Sánchez-Blázquez et al. 2006; Falcón-Barroso et al. 2011), `Cloudy` nebular emission models (Ferland et al. 2017), and Charlot & Fall's (2000) dust model with $0 < A_V < 5$ and $0.3 < n < 2.5$ as free parameters. The stellar and gas phase metallicity are tied to the same value and also included as a free parameter. The ionization parameters vary in the ranges of $-2 < \log\ Z < 0.3$ and $-3.5 < \log\ U < -1.0$. The SFH is parameterized as delayed-τ (i.e., SFR $\propto te^{-t/\tau}$) with age and τ as free parameters ($0.1\,\mathrm{Gyr} < \mathrm{age} < t_{\mathrm{universe}}$ and $0.01\,\mathrm{Gyr} < \tau < 5\,\mathrm{Gyr}$). Redshift likewise varies around the best-fitting spectroscopic redshifts (± 0.1).

The same procedure mentioned in Section 4.1 regarding the spectral calibration is applied. The sampling is performed via `PyMultinest` (Buchner et al. 2014; Feroz et al. 2019), with the default `Bagpipes` convergence criteria.

4.3. BEAGLE

The magnification-corrected spectra are in addition fitted with BayEsian Analysis of GaLaxy sEds (`BEAGLE`; Chevallard & Charlot 2016), which combines the latest version of the Bruzual & Charlot (2003) stellar population models with nebular emission templates by Gutkin et al. (2016) and assumes the Inoue et al. (2014) IGM attenuation models. Assuming a delayed-τ SFH as in our `Bagpipes` fit, but with an additional parameter to independently control the recent SFR (0–10 Myr), and a Small Magellanic Cloud dust attenuation law (Pei 1992), we leave all other `BEAGLE` parameters free to vary with uniform or log-uniform priors. The free parameters are the stellar mass $\log(M/M_\odot) \in [4, 10]$, the current (10 Myr) SFR $\log(\psi/M_\odot\ \mathrm{yr}^{-1}) \in [-2, 4]$, the maximum stellar age $\log(t_{\mathrm{age}}/\mathrm{yr}) \in [6, t_{\mathrm{universe}}]$, the star formation e-folding time $\log(\tau/\mathrm{yr}) \in [5.5, 9.5]$, the stellar metallicity $\log(Z/Z_\odot) \in [-2.2, -0.3]$, the effective V-band dust attenuation optical depth $\hat{\tau}_V \in [0, 3]$, the effective galaxy-wide ionization parameter $\log\ U \in [-4, -1]$, the gas-phase metallicity $\log(Z_{\mathrm{gas}}/Z_\odot) \in [-2.2, -0.3]$, and the dust-to-metal mass ratio $\xi_d \in [0.1, 0.5]$.

We note that `BEAGLE` does not calibrate the spectrum to the photometric data during modeling fitting. Given that the absolute flux calibration of NIRSpec is still an ongoing effort in the community, we only consider the `BEAGLE` results as a sanity check in this work.

5. Results

The redshifts and inferred stellar population parameters are summarized in Table 1. We discuss the results in more detail in the following sections.

Table 1
Ancillary Parameters

	UNCOVER-z12[a]	UNCOVER-z13[b]
R.A. (deg)	3.51356	3.57087
Decl. (deg)	−30.35680	−30.40158
z_{spec}	$12.393^{+0.004}_{-0.001}$	$13.079^{+0.013}_{-0.001}$
M_{F444W}	-18.9 ± 0.1	-18.3 ± 0.6
M_{F200W}	-19.2 ± 0.5	-19.4 ± 1.8
μ	$1.520^{+0.015}_{-0.039}$	$2.278^{+0.084}_{-0.005}$
μ_{t}	$1.511^{+0.018}_{-0.029}$	$1.881^{+0.044}_{-0.012}$
Sérsic n	$2.77^{+0.81}_{-1.04}$	$0.78^{+0.19}_{-0.09}$
`Prospector`		
$\log M/\ M_\odot$	$8.63^{+0.20}_{-0.22}$	$7.92^{+0.23}_{-0.16}$
Age (yr)	$7.76^{+0.34}_{-0.19}$	$7.65^{+0.22}_{-0.29}$
SFR ($M_\odot\ \mathrm{yr}^{-1}$)	$1.40^{+2.81}_{-1.16}$	$1.95^{+0.41}_{-0.39}$
log sSFR (yr^{-1})	$-8.69^{+0.68}_{-0.93}$	$-7.76^{+0.23}_{-0.33}$
$\log Z/Z_\odot$	$-1.40^{+0.67}_{-0.39}$	$-1.19^{+0.87}_{-0.53}$
$\hat{\tau}_{\mathrm{dust,2}}$	$0.17^{+0.34}_{-0.13}$	$0.02^{+0.04}_{-0.02}$
`Bagpipes`		
$\log M/M_\odot$	$8.35^{+0.18}_{-0.14}$	$8.13^{+0.11}_{-0.15}$
Age (yr)	$7.79^{+0.18}_{-0.15}$	$7.82^{+0.14}_{-0.17}$
SFR ($M_\odot\ \mathrm{yr}^{-1}$)	$2.15^{+0.81}_{-0.46}$	$1.28^{+0.27}_{-0.18}$
log sSFR (yr^{-1})	$-8.00^{+0.07}_{-0.11}$	$-8.01^{+0.08}_{-0.10}$
$\log Z/Z_\odot$	$-1.34^{+0.60}_{-0.42}$	$-1.57^{+0.35}_{-0.28}$
$\hat{\tau}_{\mathrm{v}}$	$0.19^{+0.17}_{-0.10}$	$0.04^{+0.08}_{-0.03}$

Notes.
[a] MSA ID 38766.
[b] MSA ID 13077.

5.1. Spectroscopic Redshifts

The strong break observed in UNCOVER-z12, seen in Figure 1, places it at $z_{\mathrm{spec}} = 12.393^{+0.004}_{-0.001}$ in the `msaexp` fits. The posterior distributions of redshift from both `Prospector` and `Bagpipes` spectrophotometric fits show well-behaved Gaussian shapes centered around the spectroscopic redshift, further supporting the $z > 12$ measurement, though here the redshift is confined to within ± 0.1 of the best-fit `msaexp` solution by construction. A careful analysis of possible emission lines results in no significant detection. However, comparing the S/N of the mean flux redward of the observed break to that blueward of the break (3.43 and −0.26, respectively) leads us to conclude that the Lyman break is prominent enough to determine the redshift without ambiguity. A forced Balmer break fit is included in Appendix B, offering further support for the high-redshift interpretation.

In UNCOVER-z13, we report a tentative spectroscopic redshift of $z_{\mathrm{spec}} = 13.079^{+0.013}_{-0.001}$. It exhibits a break feature at lower S/N, at a level that is analogous to the $z = 13.2$ galaxies discovered in JADES (Robertson et al. 2023; Curtis-Lake et al. 2023). Fits on both of the individual, manually extracted spectra, in addition to the coadded spectrum, also favor a high-redshift solution. A forced Balmer break fit likewise leads to a higher χ^2. However, while the S/N of the mean flux redward of the observed break is similar to the above case, the S/N blueward of the break is 1.05, indicating a marginal probability for a Balmer break. Without additional evidence in support of the high redshift interpretation (i.e., significant emission lines), we decide to only make a tentative redshift identification at this time.

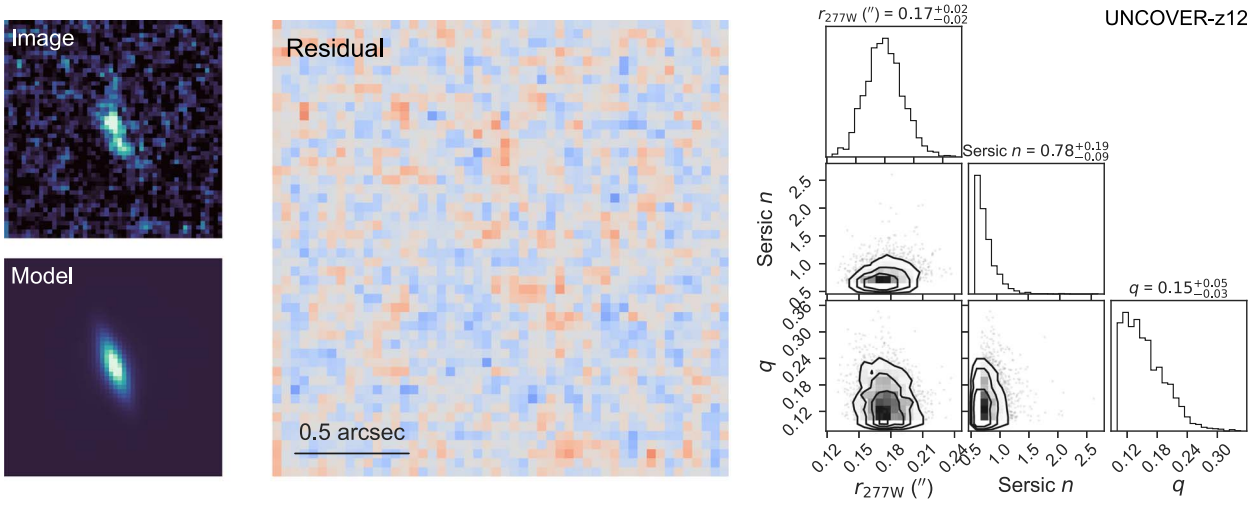

(a)

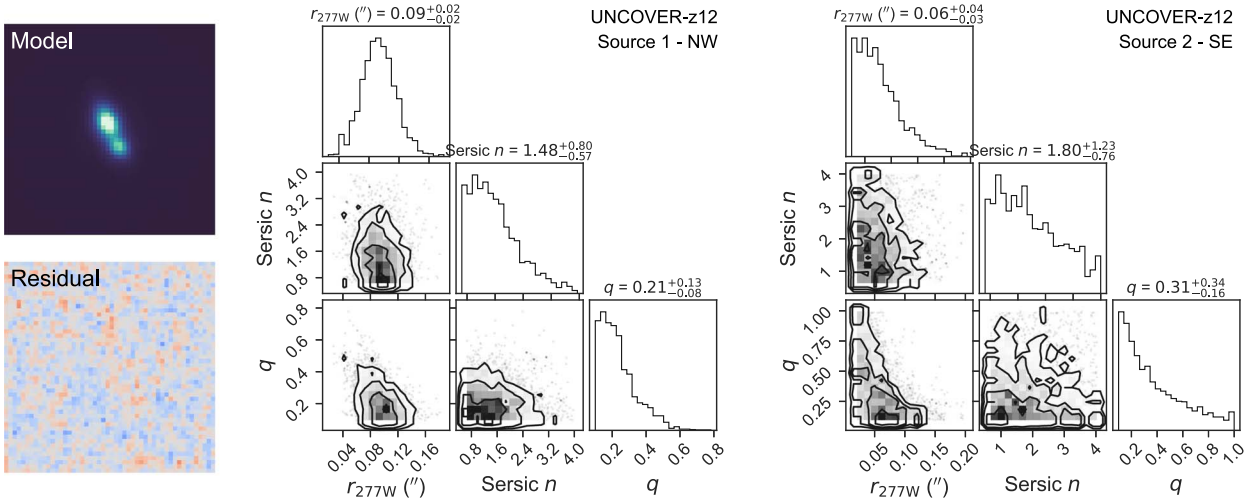

(b)

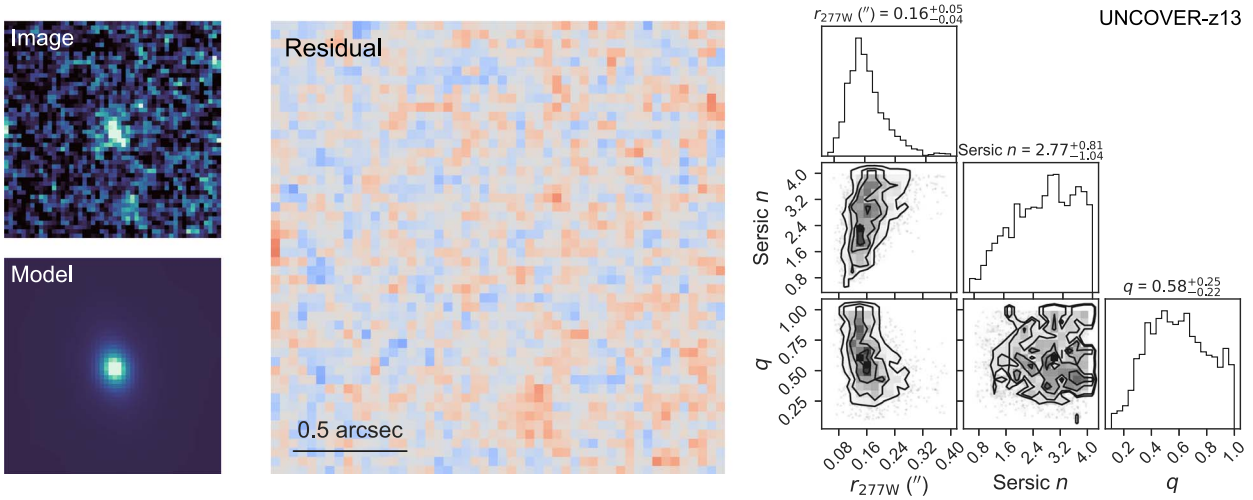

(c)

Figure 2. Morphological modeling. (a) UNCOVER-z12 is first modeled as a single source. The upper left panel shows its image in F277W, tracing recent unobscured star formation, whereas the lower left panel shows the single-component model fit. The model residual, scaled by the rms, is shown in the middle. A corner plot illustrating the posterior distributions is also included. (b) UNCOVER-z12 is also modeled as two components, and the results are presented in a similar manner. (c) Same as the first figure set, but for UNCOVER-z13.

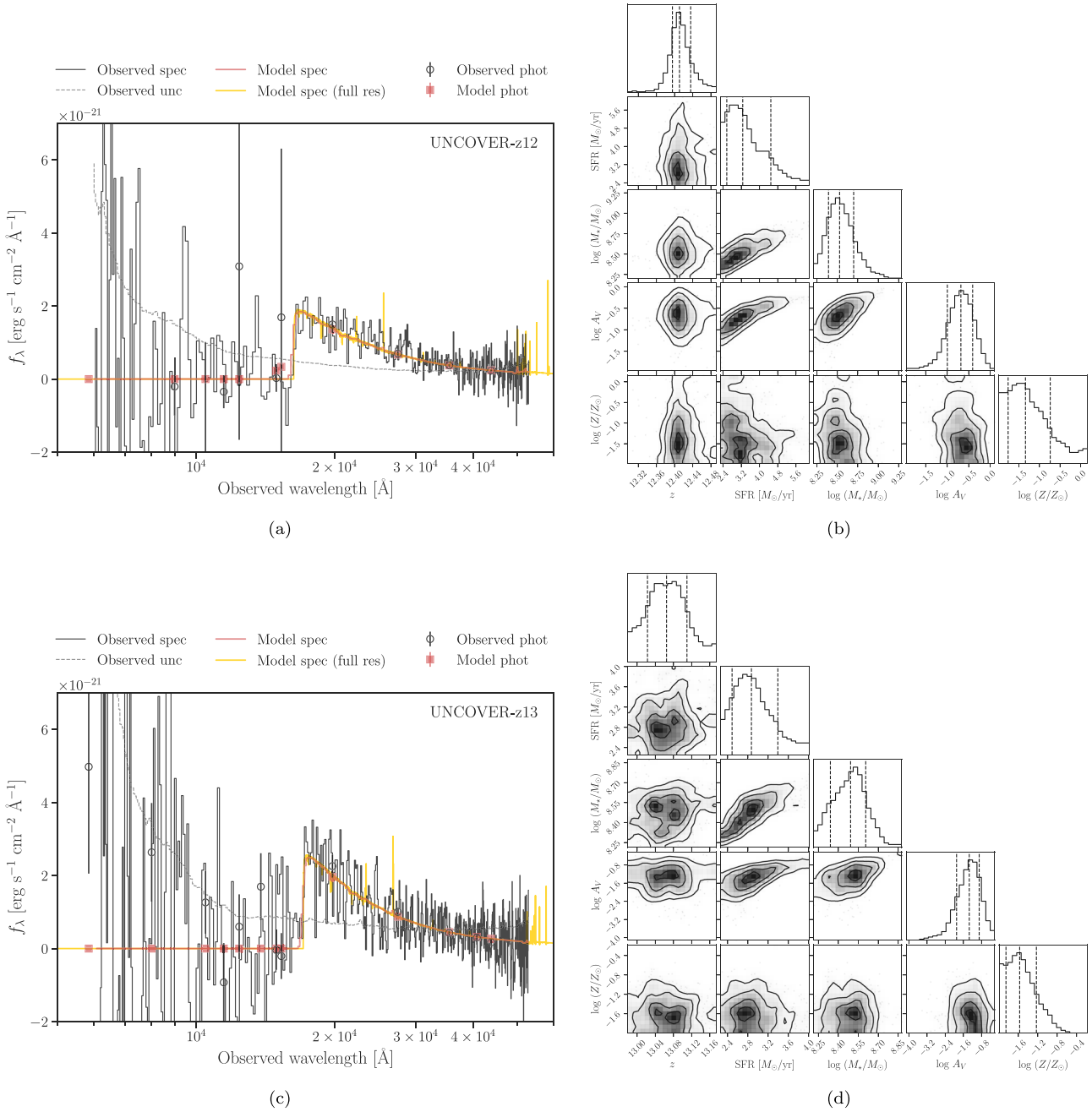

Figure 3. Stellar population modeling with `Bagpipes`. (a) The median model spectrum and photometry are shown in red, whereas the observations are shown in black. The model spectrum at the full resolution is additionally shown in gold, highlighting the predicted emission features that are washed out by the instrumental resolution. Both model spectra are scaled by a polynomial calibration vector to match the photometry. (b) The corner plot illustrates posterior distributions for a few key parameters; scale-dependent parameters are magnification-corrected. (c)–(d) Same as the above figure set, but for UNCOVER-z13. We note that the photometric data points at short wavelengths are consistent with zero flux at 1.5σ confidence.

5.2. *Morphology*

Both UNCOVER-z12 and UNCOVER-z13 are clearly resolved with measured half-light radii of $4.35^{+0.40}_{-0.39}$ pixels and $3.95^{+1.37}_{-0.94}$ pixels, respectively, with a pixel scale of $0\farcs04$ per pixel. The results are presented in Figure 2, and we elaborate on each galaxy below.

UNCOVER-z12 shows a disk-like morphology with a measured Sérsic index of $0.78^{+0.19}_{-0.09}$ and an axis ratio of $0.15^{+0.05}_{-0.03}$—this is very elongated and approaches the lower bound of the prior of 0.1. Shear boosts the semimajor axis by $\mu_t = 1.52^{+0.02}_{-0.03}$, and has roughly no effect on the semiminor axis, based on the lens model (Furtak et al. 2023). This suggests an intrinsic axis ratio of $\sim$0.23. There appears to be two main clumps in the F277W image of UNCOVER-z12, which can contribute to the extended size. In F444W, the galaxies show a much smoother distribution with a Sérsic fit that leads to similar constraints. There are no obvious systematic differences in the residuals from the Sérsic fit to the F277W image. The disturbed morphology can be driven by clumpy ongoing star formation, as it is more prevalent at shorter wavelengths.

However, an ongoing merger could also explain the clumpy morphology, we thus model UNCOVER-z12 with two Sérsic

components simultaneously as shown in Figure (2b). We find the brighter Source-1 in the NW contains about 2/3 of the total flux of the system, which remains resolved but with a half-light radius roughly half of that implied by the single Sérsic fit. Source-1 remains elongated along a similar axis and still shows disk morphology with a Sérsic index consistent with one and a lensing-corrected axis ratio of 0.31. Source-2 in the SE is much fainter, resulting in a 1σ upper limit on the size of about 1.5 pixels, or $0\farcs06$. Its Sérsic index and axis ratio are unconstrained. We note that the resulting χ^2 values are nearly identical when comparing the single Sérsic fit to the two Sérsic fits, with the latter being lower by only 2%. With both cases being physically plausible, and neither being preferred by the data, we consider both as limiting cases for the remainder of the study.

As for UNCOVER-z13, it has a Sérsic index of $2.77^{+0.81}_{-1.04}$ with a poorly constrained axis ratio of $0.58^{+0.25}_{-0.21}$. Similarly, shear boosts the semimajor axis by $\sim$1.9, and the semiminor axis by $\sim$1.5.

5.3. Stellar Populations

The different galaxy SED-fitting codes in general agree on the inferred properties for both objects, details of which are listed in Table 1. The best-fit model spectra from `Bagpipes`, alongside posterior distributions of key parameters, are shown in Figure 3. All model parameters are corrected for the magnification factor, μ. Both galaxies are moderately magnified with $\mu \sim 2$, meaning that the observed uncertainties of the photometric and spectral fluxes dominate. We find the galaxies of this work have low stellar masses of $\sim 10^8 M_\odot$, similar to the others discovered at these redshifts (e.g., Robertson et al. 2023). They are young and metal-poor; the metallicity constraints, while highly uncertain, are slightly higher than the similar spectroscopically confirmed $z > 10$ systems presented in Curtis-Lake et al. (2023). The solutions also favor fairly low dust content ($A_V \sim 0.1$) and high specific SFRs ($\log \mathrm{sSFR/yr} \sim -8$), comparable to other high-redshift systems.

In brief, these characteristics are in alignment with our expectations of early galaxies. For example, for $z \sim 12.2$ sources with $M_* \sim 10^{7.9-8.4} M_\odot$, semianalytic galaxy formation models DELPHI (Dayal et al. 2014; Mauerhofer & Dayal 2023), base-lined against data at $z \sim 5$–10, would predict SFRs between 0.8 and 3 $M_\odot \mathrm{yr}^{-1}$ and associated gas-phase metallicity values between -1.8 and -0.8. At $z \sim 13$, for $M_* \sim 10^{7.6-8.1} M_\odot$, this model would predict SFR between 0.5 and 2.6 $M_\odot \mathrm{yr}^{-1}$ and associated gas-phase metallicities between -1.8 and -0.9, in $\log_{10}$ units relative to solar metallicity. Within uncertainties, these values are in good agreement with those inferred from our SED fitting, suggesting that these galaxies lie on or close to the values expected for main-sequence systems at these early epochs.

6. Discussion and Conclusions

This Letter presents spectroscopic observations of two galaxies using NIRSpec/Prism onboard JWST. We summarize the main findings as follows.

UNCOVER-z12 is located securely at $z_{\mathrm{spec}} = 12.393^{+0.004}_{-0.001}$ due to an unambiguous Lyman break, placing it as the fourth most distant, spectroscopically confirmed galaxy known to date; UNCOVER-z13 is tentatively detected at $z_{\mathrm{spec}} = 13.079^{+0.013}_{-0.001}$.

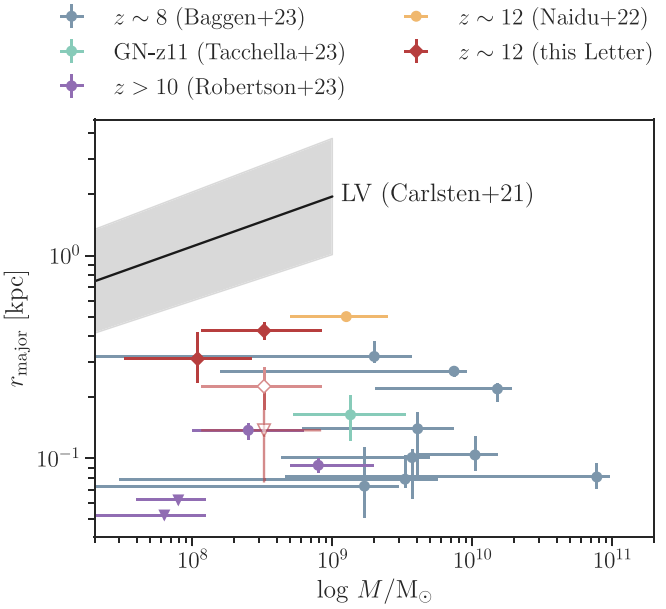

Figure 4. Mass–size relationship. UNCOVER-z12 and UNCOVER-z13 are shown as red diamonds. We take the average masses and uncertainties from the three SED fitting results. Also shown in unfilled red symbols are the UNCOVER-z12 sizes assuming two components. The triangle indicates an upper limit. We include five data sets from the literature as well: massive galaxies at $z \sim 8$ (Baggen et al. 2023; Labbé et al. 2023), GN-z11 at $z \sim 11$ (Tacchella et al. 2023), a plausible luminous galaxy at $z \sim 12$ (Naidu et al. 2022b; Bakx et al. 2023), and $z > 10$ galaxies confirmed by JADES (Curtis-Lake et al. 2023; Robertson et al. 2023). The gray line is a fit of the mass–size relationship for satellites of Milky Way–like hosts (Carlsten et al. 2021); note that the local volume (LV) relation is measured at different rest-frame wavelengths than the high-redshift samples, and is included here only for reference. The galaxies of this Letter are among the largest known at $z \gtrsim 10$.

We err on the conservative side and do not firmly rule out a lower-redshift solution for UNCOVER-z13 for two reasons: first, the break is weaker, and thus possibly instead a Balmer break; second, the emission features seen in the spectrum are consistent with noise, providing no additional evidence in support of a $z \sim 13$ interpretation.

Stellar population modeling is performed using independent codes, all constrained by the same HST+JWST photometric and JWST/NIRSpec spectroscopic observations. The inferred galaxy properties are consistent with expectations of early systems: low mass ($\sim 10^8 M_\odot$), young, rapidly assembling, metal-poor, and star-forming.

As both galaxies are clearly spatially resolved, we are able to make reliable morphological measurements. The shear-corrected effective radii are 426^{+40}_{-42} pc and 309^{+110}_{-74} pc for UNCOVER-z12 and UNCOVER-z13, respectively. The resulting SFR surface densities are $\sim 2.45 \pm 0.85$ and $1.68 \pm 1.00\, M_\odot \mathrm{yr}^{-1} \mathrm{kpc}^{-2}$, which are less extreme than the 15—180 $M_\odot \mathrm{yr}^{-1} \mathrm{kpc}^{-2}$ range reported in Robertson et al. (2023). In addition, UNCOVER-z12 exhibits a disturbed morphology, indicating clumpy star formation (Marshall et al. 2022; Chen et al. 2023; Trussler et al. 2023). We thus consider an alternative merger scenario, which is likely in the context of hierarchical structure formation (White & Frenk 1991). This interaction would trigger star formation, manifesting as burstiness in the inferred SFH. With that being said, the observations place limited constraints on the SFH, offering no additional evidence for or against the merger hypothesis.

Nevertheless, we model the two components separately for completeness. The shear-corrected effective radius for the NW source is 227^{+55}_{-53} pc, and an upper limit for the SE source is 138^{+95}_{-62} pc.

We place the morphological measurements in the context of other high-redshift samples in Figure 4. Interestingly, the galaxies of this Letter are notably larger than the $z > 10$ galaxies reported in Robertson et al. (2023) and are comparable to the massive galaxies at $z \sim 8$ (Baggen et al. 2023; Labbé et al. 2023). These measurements may hint at a scatter in the mass–size relationship at early epochs, and that selection effects could bias samples toward the most compact objects in shallower surveys.

To conclude, the earliest galaxies are crucial in understanding the theories of galaxy and structure formation, yet only three $z > 12$ galaxies have been confirmed in the literature thus far (Bakx et al. 2023; Curtis-Lake et al. 2023; Robertson et al. 2023). The discoveries presented here therefore provide valuable insights into a redshift space now accessible by JWST. It is hopeful that future systematic searches and investigations in this observational frontier will fill in one of the last missing pieces in modern astrophysics: the nature of the first luminous sources and their large-scale impact.

Acknowledgments

This work is based, in part, on observations made with the NASA/ESA/CSA James Webb Space Telescope. The data were obtained from the Mikulski Archive for Space Telescopes at the Space Telescope Science Institute, which is operated by the Association of Universities for Research in Astronomy, Inc. (AURA), under NASA contract NAS 5-03127 for JWST. These observations are associated with JWST-GO-2561, JWST-ERS-1324, and JWST-DD-2756. This research is also based on observations made with the NASA/ESA Hubble Space Telescope obtained from the Space Telescope Science Institute under NASA contract NAS 526555. These observations are associated with programs HST-GO-11689, HST-GO-13386, HST-GO/DD-13495, HST-GO-13389, HST-GO-15117, and HST-GO/DD-17231. The specific observations analyzed can be accessed via 10.17909/8k5c-xr27.

B.W. thanks Ben Johnson for discussions on the size measurements of the JADES galaxies. B.W. and J.L. acknowledge support from JWST-GO-02561.022-A. A.Z. and L.J.F. acknowledge support by grant 2020750 from the United States-Israel Binational Science Foundation (BSF) and grant 2109066 from the United States National Science Foundation (NSF), and by the Ministry of Science & Technology, Israel. H.A. and I.C. acknowledge support from CNES, focused on the JWST mission, and the Programme National Cosmology and Galaxies (PNCG) of CNRS/INSU with INP and IN2P3, cofunded by CEA and CNES. R.B. acknowledges support from the Research Corporation for Scientific Advancement (RCSA) Cottrell Scholar Award ID No: 27587. P.D. acknowledges support from the NWO grant 016.VIDI.189.162 ("ODIN") and the European Commission's and University of Groningen's CO-FUND Rosalind Franklin program. J.E.G. acknowledges NSF/AAG grant# 1007094. Y.F. acknowledges support from NAOJ ALMA Scientific Research grant No. 2020-16B, and from JSPS KAKENHI grant No. JP23K13149. R.P. and D.M. acknowledge support from JWST-GO-02561.013-A. The work of C.C.W. is supported by NOIRLab, which is managed by AURA under a cooperative agreement with the NSF. The Cosmic Dawn Center is funded by the Danish National Research Foundation (DNRF) under grant #140.

Computations for this research were performed on the Pennsylvania State University's Institute for Computational and Data Sciences' Roar supercomputer. This publication made use of the NASA Astrophysical Data System for bibliographic information.

Facilities: HST(ACS, WFC3), JWST(NIRCam, NIRSpec).

Software: Astropy (Astropy Collaboration et al. 2013, 2018, 2022), Bagpipes (Carnall et al. 2018, 2019), BEAGLE (Chevallard & Charlot 2016), Cloudy (Ferland et al. 2017), Corner (Foreman-Mackey 2016), EAzY (Brammer et al. 2008), FSPS (Conroy & Gunn 2010), dynesty (Speagle 2020), Matplotlib (Hunter 2007), msaexp (Brammer et al. 2022, v0.6.10), NumPy (Harris et al. 2020), NUTS (Hoffman & Gelman 2011; Phan et al. 2019), Prospector (Johnson et al. 2021), PyMultinest (Buchner et al. 2014; Feroz et al. 2019), pysersic (Pasha & Miller 2023), SciPy (Virtanen et al. 2020).

Appendix A
Parent Sample

We supplement further details on the parent sample. Table B1 lists all the candidates that show photometric redshifts >12, but were not confirmed to be high-redshift after the spectroscopic observations due to various reasons also noted in the table. Figure A1 includes all the spectra, accompanied by $p(z)$.

Out of a total of eight candidates, three turn out to be too faint to infer the nature of the sources. One candidate may be affected by the modeling of the brightest cluster galaxies in the vicinity and has been deemed as an artifact in later iterations of the photometric reduction pipeline. For the remaining two failed candidates, one exhibits a plausible emission line, which leads us to favor a low-redshift solution, whereas the other candidate is a textbook example of confusion between Lyman and Balmer breaks. The S/N of the mean flux red- and blueward of the break are 4.77 and 2.65, respectively, corroborating the Balmer break diagnostic.

It is also interesting to revisit the prespectra photometric redshifts. `EAzY` identifies all eight candidates at $z > 11$. Medians of the redshift posteriors from `Prospector` places one of them at low redshift, whereas the maximum-likelihood redshifts indicate four of them are better fitted with a low-redshift model. The latter suggests that it is possible to improve the photometric inference via more informative priors. The effect of including a number density prior, as proposed in Wang et al. (2023), will be explored in the next generation of stellar population catalogs as part of the UNCOVER survey.

Finally, a word of caution: it is too early to draw conclusions about selection effects or success rates; here we merely aim to paint a more complete picture of the sample.

Table B1
Low-redshift Interlopers or Unconfirmed Sources

ID	R.A. (deg)	Decl. (deg)	$z_{\rm eazy}$[a]	$z_{\rm med,sps}$[b]	$z_{\rm ml,sps}$[c]	Notes
13805	3.56699	−30.39996	$11.38^{+0.28}_{-8.45}$	$11.58^{+0.54}_{-9.78}$	2.21	low-z emission line
22002	3.63043	−30.38362	$11.42^{+1.67}_{-7.85}$	$13.55^{+2.59}_{-9.42}$	3.38	low S/N
40411	3.57991	−30.35699	$15.20^{+0.29}_{-0.75}$	$15.81^{+0.44}_{-0.50}$	16.28	data quality issue
44644	3.58291	−30.34601	$14.18^{+0.28}_{-2.14}$	$14.24^{+0.91}_{-1.74}$	15.01	Balmer break
45390	3.55640	−30.34433	$15.68^{+0.56}_{-11.01}$	$15.36^{+1.17}_{-11.22}$	4.88	low S/N
51704	3.55716	−30.32870	$11.63^{+0.21}_{-8.88}$	$1.86^{+0.54}_{-9.78}$	3.02	low S/N

Notes.
[a] Photometric redshift from `EAzY`.
[b] Posterior median of photometric redshift from `Prospector`.
[c] Maximum-likelihood photometric redshift from `Prospector`.

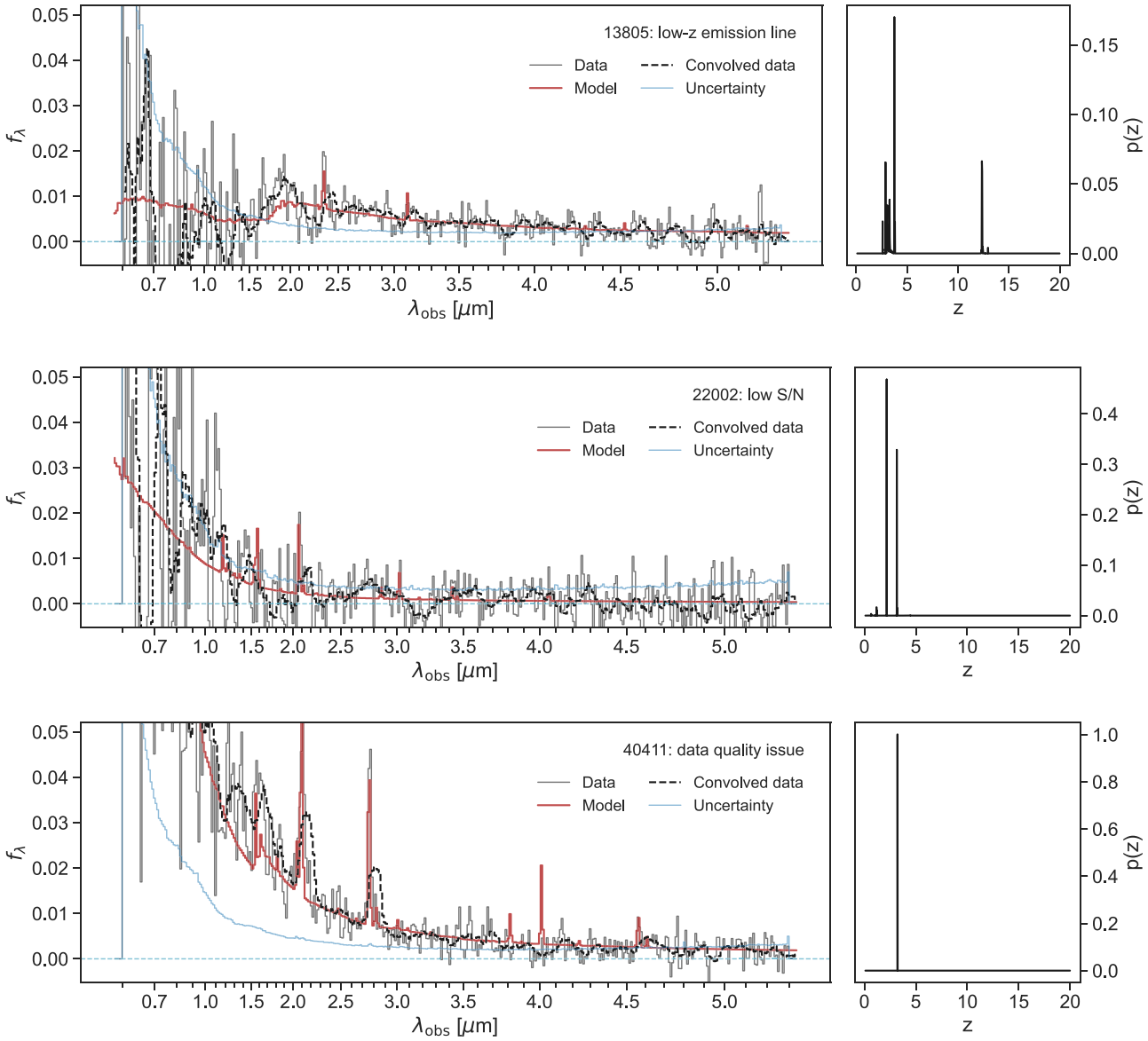

Figure A1. Low-redshift interlopers or unconfirmed sources. For each figure, the left panel displays the 1D spectrum in $f\lambda$ as a function of the observed wavelength. Data, the best-fit EAzY model, and uncertainties are plotted in gray, red, and blue, respectively. A convolved observed spectrum is additionally shown as a dashed black line for visualization purposes. The cyan horizontal line is at $y = 0$ to guide the eye. The right panel shows the probability density over the redshift range of the search for a minimum χ^2.

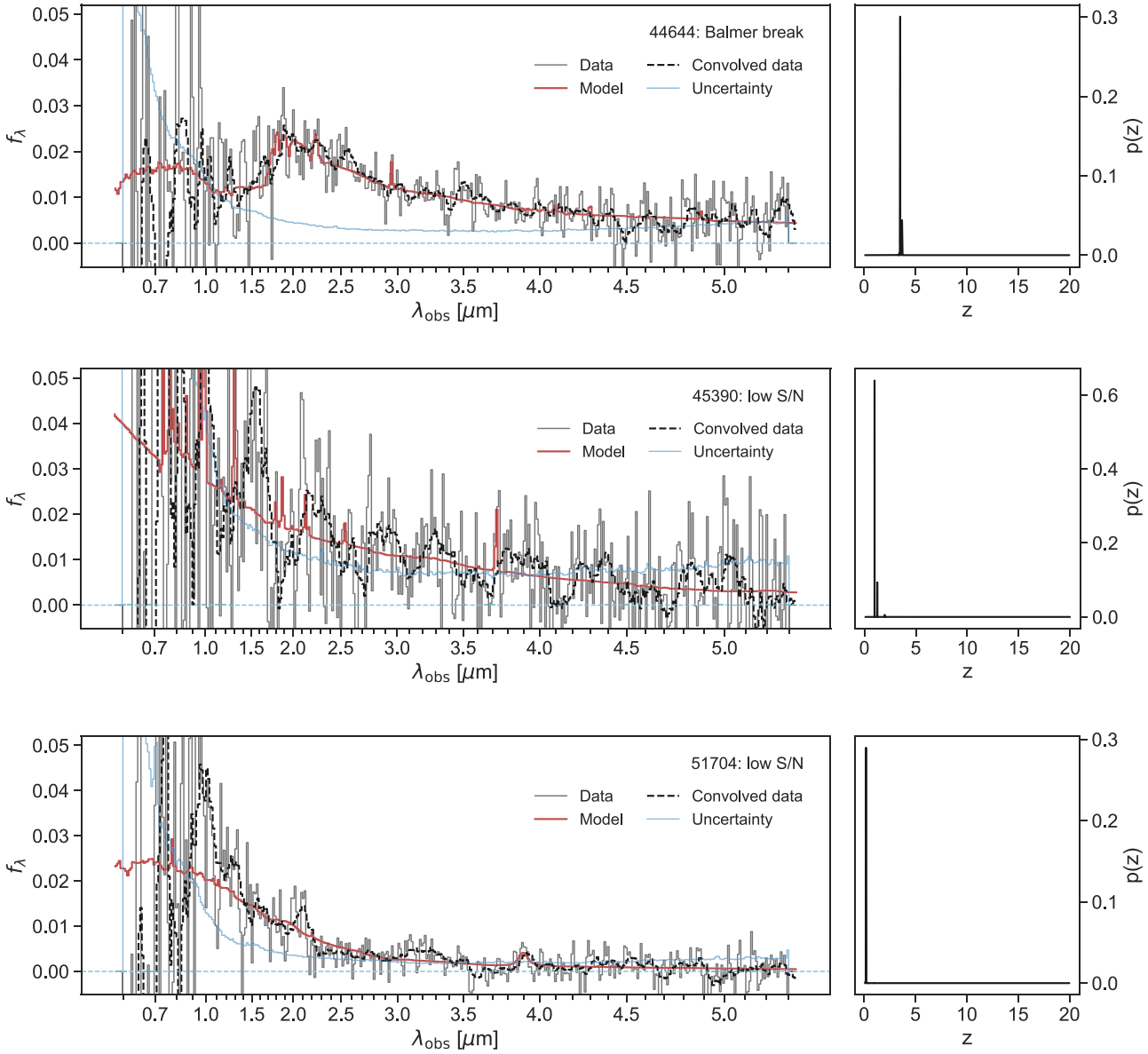

Figure A1. (Continued.)

Appendix B
Forced Fits at Low Redshift

We fit the observed spectra by adapting the same procedure outlined in Section 3.1, but restricting the redshift range to be $0 < z < 10$. The best-fit model spectra and $p(z)$ are shown in Figure B1.

In addition, we compare the χ^2 values between the best-fit models from `Bagpipes` at high and low redshifts. Similar to the findings above, the $z > 12$ solutions are preferred for both sources.

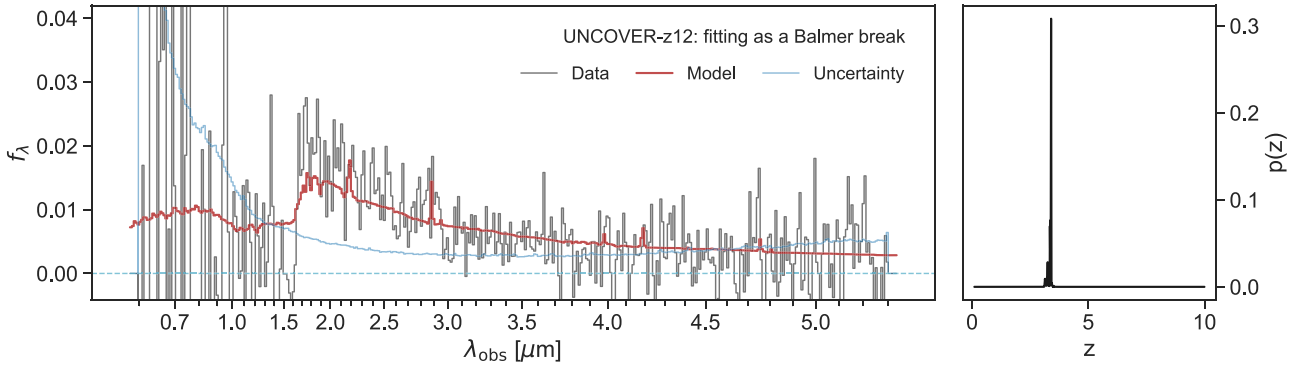

(a)

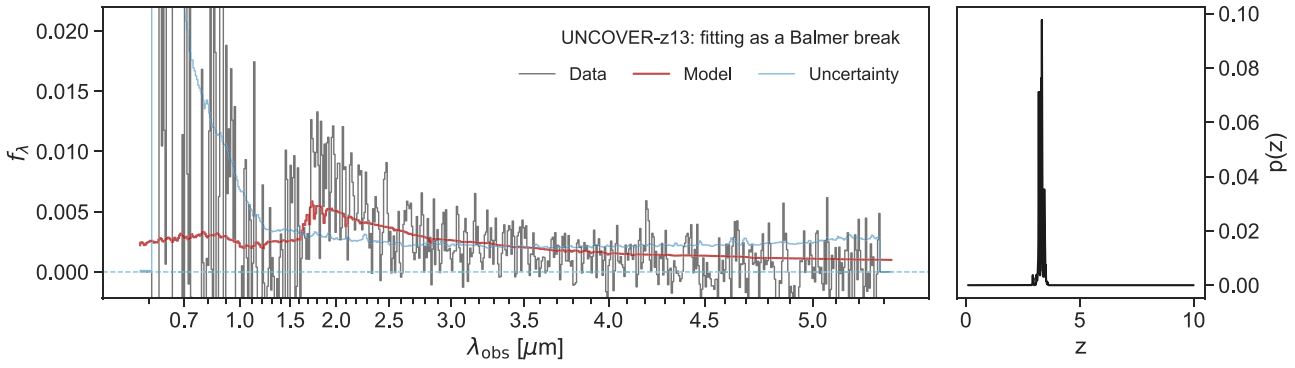

(b)

Figure B1. Forced fits at low redshift. (a) The left panel displays the 1D spectrum for UNCOVER-z12 in f_λ as a function of the observed wavelength. Data are plotted in gray, whereas the best-fit EAzY model at $z \sim 3$ is plotted in red. Also plotted are the uncertainties in blue. The cyan horizontal line is at $y = 0$ to guide the eye. The right panel shows the probability density over the redshift range of the search for a minimum χ^2. (b) Same as the above figure, but for UNCOVER-z13. The high-redshift solutions are favored for both sources.

ORCID iDs

Bingjie Wang (王冰洁) https://orcid.org/0000-0001-9269-5046
Seiji Fujimoto https://orcid.org/0000-0001-7201-5066
Ivo Labbé https://orcid.org/0000-0002-2057-5376
Lukas J. Furtak https://orcid.org/0000-0001-6278-032X
Tim B. Miller https://orcid.org/0000-0001-8367-6265
David J. Setton https://orcid.org/0000-0003-4075-7393
Adi Zitrin https://orcid.org/0000-0002-0350-4488
Hakim Atek https://orcid.org/0000-0002-7570-0824
Rachel Bezanson https://orcid.org/0000-0001-5063-8254
Gabriel Brammer https://orcid.org/0000-0003-2680-005X
Joel Leja https://orcid.org/0000-0001-6755-1315
Pascal A. Oesch https://orcid.org/0000-0001-5851-6649
Sedona H. Price https://orcid.org/0000-0002-0108-4176
Iryna Chemerynska https://orcid.org/0009-0009-9795-6167
Sam E. Cutler https://orcid.org/0000-0002-7031-2865
Pratika Dayal https://orcid.org/0000-0001-8460-1564
Pieter van Dokkum https://orcid.org/0000-0002-8282-9888
Andy D. Goulding https://orcid.org/0000-0003-4700-663X
Jenny E. Greene https://orcid.org/0000-0002-5612-3427
Y. Fudamoto https://orcid.org/0000-0001-7440-8832
Gourav Khullar https://orcid.org/0000-0002-3475-7648
Vasily Kokorev https://orcid.org/0000-0002-5588-9156
Danilo Marchesini https://orcid.org/0000-0001-9002-3502
Richard Pan https://orcid.org/0000-0002-9651-5716
John R. Weaver https://orcid.org/0000-0003-1614-196X
Katherine E. Whitaker https://orcid.org/0000-0001-7160-3632
Christina C. Williams https://orcid.org/0000-0003-2919-7495

References

Arrabal Haro, P., Dickinson, M., Finkelstein, S. L., et al. 2023a, ApJL, 951, L22
Arrabal Haro, P., Dickinson, M., Finkelstein, S. L., et al. 2023b, arXiv:2303.15431
Astropy Collaboration, Price-Whelan, A. M., Lim, P. L., et al. 2022, ApJ, 935, 167
Astropy Collaboration, Price-Whelan, A. M., Sipőcz, B. M., et al. 2018, AJ, 156, 123
Astropy Collaboration, Robitaille, T. P., Tollerud, E., et al. 2013, A&A, 558, A33
Atek, H., Chemerynska, I., Wang, B., et al. 2023, MNRAS, 524, 5486
Baggen, J. F. W., van Dokkum, P., Labbe, I., et al. 2023, ApJL, 955, L12
Bakx, T. J. L. C., Zavala, J. A., Mitsuhashi, I., et al. 2023, MNRAS, 519, 5076
Barbary, K., Boone, K., McCully, C., et al. 2016, Kbarbary/Sep: v1.0.0, Zenodo, doi:10.5281/zenodo.159035
Bergamini, P., Acebron, A., Grillo, C., et al. 2023, ApJ, 952, 84
Bertin, E., & Arnouts, S. 1996, A&AS, 117, 393
Bezanson, R., Labbe, I., Whitaker, K. E., et al. 2022, arXiv:2212.04026
Brammer, G., Strait, V., Matharu, J., & Momcheva, I. 2022, grizli, v1.5.0, Zenodo, doi:10.5281/zenodo.6672538
Brammer, G. B., van Dokkum, P. G., & Coppi, P. 2008, ApJ, 686, 1503
Bromm, V., & Yoshida, N. 2011, ARA&A, 49, 373
Bruzual, G., & Charlot, S. 2003, MNRAS, 344, 1000
Buchner, J., Georgakakis, A., Nandra, K., et al. 2014, A&A, 564, A125
Bunker, A. J., Saxena, A., Cameron, A. J., et al. 2023, A&A, 677, A88

Carlsten, S. G., Greene, J. E., Peter, A. H. G., Beaton, R. L., & Greco, J. P. 2021, ApJ, 908, 109
Carnall, A. C., McLure, R. J., Dunlop, J. S., et al. 2019, MNRAS, 490, 417
Carnall, A. C., McLure, R. J., Dunlop, J. S., & Davé, R. 2018, MNRAS, 480, 4379
Chabrier, G. 2003, PASP, 115, 763
Charlot, S., & Fall, S. M. 2000, ApJ, 539, 718
Chen, Z., Stark, D. P., Endsley, R., et al. 2023, MNRAS, 518, 5607
Chevallard, J., & Charlot, S. 2016, MNRAS, 462, 1415
Choi, J., Dotter, A., Conroy, C., et al. 2016, ApJ, 823, 102
Conroy, C., & Gunn, J. E. 2010, ApJ, 712, 833
Curtis-Lake, E., Carniani, S., Cameron, A., et al. 2023, NatAs, 7, 622
Dayal, P., Ferrara, A., Dunlop, J. S., & Pacucci, F. 2014, MNRAS, 445, 2545
Dotter, A. 2016, ApJS, 222, 8
Dunlop, J. S., Cirasuolo, M., & McLure, R. J. 2007, MNRAS, 376, 1054
Falcón-Barroso, J., Sánchez-Blázquez, P., Vazdekis, A., et al. 2011, A&A, 532, A95
Fan, X., Strauss, M. A., Becker, R. H., et al. 2006, AJ, 132, 117
Ferland, G. J., Chatzikos, M., Guzmán, F., et al. 2017, RMxAA, 53, 385
Feroz, F., Hobson, M. P., Cameron, E., & Pettitt, A. N. 2019, JAp, 2, 10
Foreman-Mackey, D. 2016, JOSS, 1, 24
Fujimoto, S., Arrabal Haro, P., Dickinson, M., et al. 2023, ApJL, 949, L25
Furtak, L. J., Zitrin, A., Weaver, J. R., et al. 2023, MNRAS, 523, 4568
Gunn, J. E., & Peterson, B. A. 1965, ApJ, 142, 1633
Gutkin, J., Charlot, S., & Bruzual, G. 2016, MNRAS, 462, 1757
Harris, C. R., Millman, K. J., van der Walt, S. J., et al. 2020, Natur, 585, 357
Hinshaw, G., Larson, D., Komatsu, E., et al. 2013, ApJS, 208, 19
Hoffman, M. D., & Gelman, A. 2011, arXiv:1111.4246
Hunter, J. D. 2007, CSE, 9, 90
Inayoshi, K., Visbal, E., & Haiman, Z. 2020, ARA&A, 58, 27
Inoue, A. K., Shimizu, I., Iwata, I., & Tanaka, M. 2014, MNRAS, 442, 1805
Johnson, B. D., Leja, J., Conroy, C., & Speagle, J. S. 2021, ApJS, 254, 22
Klessen, R. S., & Glover, S. C. O. 2023, ARA&A, 61, 65
Labbé, I., van Dokkum, P., Nelson, E., et al. 2023, Natur, 616, 266
Leja, J., Johnson, B. D., Conroy, C., van Dokkum, P. G., & Byler, N. 2017, ApJ, 837, 170
Lotz, J. M., Koekemoer, A., Coe, D., et al. 2017, ApJ, 837, 97
Madau, P., & Dickinson, M. 2014, ARA&A, 52, 415
Marshall, M. A., Wilkins, S., Di Matteo, T., et al. 2022, MNRAS, 511, 5475
Mauerhofer, V., & Dayal, P. 2023, MNRAS, 526, 2196
McKinney, J., Finnerty, L., Casey, C. M., et al. 2023, ApJL, 946, L39
McQuinn, M. 2016, ARA&A, 54, 313
Naidu, R. P., Oesch, P. A., Setton, D. J., et al. 2022a, arXiv:2208.02794
Naidu, R. P., Oesch, P. A., van Dokkum, P., et al. 2022b, ApJL, 940, L14
Oesch, P. A., Brammer, G., van Dokkum, P. G., et al. 2016, ApJ, 819, 129
Pasha, I., & Miller, T. B. 2023, arXiv:2306.05454
Pei, Y. C. 1992, ApJ, 395, 130
Phan, D., Pradhan, N., & Jankowiak, M. 2019, arXiv:1912.11554
Planck Collaboration, Aghanim, N., Akrami, Y., et al. 2020, A&A, 641, A6
Rigby, J., Perrin, M., McElwain, M., et al. 2023, PASP, 135, 048001
RobertsBorsani, G., Treu, T., Chen, W., et al. 2023, Natur, 618, 480
Robertson, B. E. 2022, ARA&A, 60, 121
Robertson, B. E., Tacchella, S., Johnson, B. D., et al. 2023, NatAs, 7, 611
Sánchez-Blázquez, P., Peletier, R. F., Jiménez-Vicente, J., et al. 2006, MNRAS, 371, 703
Speagle, J. S. 2020, MNRAS, 493, 3132
Stark, D. P. 2016, ARA&A, 54, 761
Steinhardt, C. L., Jauzac, M., Acebron, A., et al. 2020, ApJS, 247, 64
Tacchella, S., Eisenstein, D. J., Hainline, K., et al. 2023, ApJ, 952, 74
Treu, T., RobertsBorsani, G., Bradac, M., et al. 2022, ApJ, 935, 110
Trussler, J. A. A., Adams, N. J., Conselice, C. J., et al. 2023, MNRAS, 523, 3423
Virtanen, P., Gommers, R., Oliphant, T. E., et al. 2020, NatMe, 17, 261
Wang, B., Leja, J., Bezanson, R., et al. 2023, ApJL, 944, L58
Wang, B., Leja, J., & Labbé, I. 2023, arXiv:2310.01276
Weaver, J. R., Cutler, S. E., Pan, R., et al. 2023, arXiv:2301.02671
White, S. D. M., & Frenk, C. S. 1991, ApJ, 379, 52
Williams, H., Kelly, P. L., Chen, W., et al. 2023, Sci, 380, 416
Zavala, J. A., Buat, V., Casey, C. M., et al. 2023, ApJL, 943, L9